Bias from gas inhomogeneities in the pressure profiles as measured from X-ray and SZ observations

S. Khedekar[1]*, E. Churazov[1,2], A. Kravtsov[3,4], I. Zhuravleva[1,5], E.T. Lau[6,7], D. Nagai[6,7], R. Sunyaev[1,2]

[1] *MPI für Astrophysik, Karl-Schwarzschild str. 1, Garching, 85741, Germany*
[2] *Space Research Institute, Profsoyuznaya str. 84/32, Moscow, 117997, Russia*
[3] *Department of Astronomy and Astrophysics, University of Chicago, 5640 South Ellis Avenue, Chicago, IL 60637, USA*
[4] *Kavli Institute for Cosmological Physics and Enrico Fermi Institute, University of Chicago, Chicago, IL 60637, USA*
[5] *Kavli Institute for Particle Astrophysics and Cosmology, Stanford University, 452 Lomita Mall, Stanford, CA 94305-4085, USA*
[6] *Department of Physics, Yale University, New Haven, CT 06520, USA*
[7] *Yale Center for Astronomy and Astrophysics, Yale University, New Haven, CT 06520, USA*

Draft: 6 February 2013

ABSTRACT

X-ray observations of galaxy clusters provide emission measure weighted spectra, arising from a range of density and temperature fluctuations in the intra-cluster medium (ICM). This is fitted to a single temperature plasma emission model to provide an estimate of the gas density and temperature, which are sensitive to the gas inhomogeneities. Therefore, X-ray observations yield a potentially biased estimate of the thermal gas pressure, P_X. At the same time Sunyaev-Zeldovich (SZ) observations directly measure the integrated gas pressure, P_{SZ}. If the X-ray pressure profiles are strongly biased with respect to the SZ, then one has the possibility to probe the gas inhomogeneities (their amplitude and physical nature), even at scales unresolved by the current generation of telescopes. At the same time, a weak bias has implications for the interchangeable use of mass proxies like Y_{SZ} and Y_X as cosmological probes. In this paper we investigate the dependence of the bias, defined as $b_P(r) \equiv P_X(r)/P_{SZ}(r) - 1$, on the characteristics of fluctuations in the ICM taking into account the correlation between temperature and density fluctuations. We made a simple prediction of the *irreducible* bias in idealised X-ray vs SZ observations using multi-temperature plasma emission model. We also provide a simple fitting form to estimate the bias given the distribution of fluctuations. In real observations there can be additional complications arising from instrumental background, insufficient photon statistics, asphericity, method of deprojection, etc. Analysing a sample of 16 clusters extracted from hydrodynamical simulations, we find that the median value of bias is within $\pm 3\%$ within R_{500}, it decreases to -5% at $R_{500} < r < 1.5\ R_{500}$ and then rises back to $\sim 0\%$ at $r \gtrsim 2\ R_{500}$. The scatter of $b_P(r)$ between individual relaxed clusters is small – at the level of < 0.03 within R_{500}, but turns significantly larger (0.25) and highly skewed ($\bar{b}_P(r) \gg 0$) at $r \gtrsim 1.5\ R_{500}$. For any relaxed cluster we find $|b_P(r)| < 15\%$ within R_{500}, across different implementations of input physics in the simulations. Unrelaxed clusters exhibit a larger scatter in $b_P(r)$ (both from radius to radius and from cluster to cluster).

Key words: galaxies: clusters: intra-cluster medium — X-rays: galaxies: clusters — cosmic background radiation

1 INTRODUCTION

Galaxy clusters offer an interesting possibility of probing physics relevant on both cosmological as well as galactic scales (see recent review by Kravtsov & Borgani

* satej@mpa-garching.mpg.de

2012). On the one hand, they are useful for constraining cosmological parameters (Haiman et al. 2001), models of dark energy (Majumdar & Mohr 2004; Vikhlinin et al. 2009; Burenin & Vikhlinin 2012), and possible modifications to the theory of gravity (Rapetti et al. 2009). At the same time, they offer insights into feedback processes involving the interplay between the intra-cluster medium (ICM) and constituent galaxies, and growth of supermassive black holes occurring at their centres (e.g., Churazov et al. 2005; Croton et al. 2006; Rafferty et al. 2006; Somerville et al. 2008).

Galaxy clusters emit strongly in X-rays from the shock heating and compression of the infalling matter (Sunyaev & Zeldovich 1972a). In the last two decades, a large number clusters have been imaged at high resolution through X-ray instruments such as ROSAT, XMM-Newton and Chandra. The X-ray satellite, Suzaku has also been useful at imaging the outskirts of clusters (e.g., Simionescu et al. 2011), due to its lower instrumental background. On the cosmic microwave background (CMB) sky, clusters are visible due to the inverse Compton scattering of the CMB photons by the hot ICM, known commonly as the SZ effect (Sunyaev & Zeldovich 1972b). In recent years ongoing SZ surveys like SPT (Reichardt et al. 2012), ACT (Marriage et al. 2011), Planck (Planck Collaboration et al. 2011a) and BOLOCAM (Sayers et al. 2012) have been imaging clusters on arc-minute scales using multi-frequency data. These surveys should detect $\gtrsim 1000$ clusters up to high redshifts making them valuable as cosmological probes. However, in order to place competitive constraints from these observations, the cluster masses would have to be determined with an accuracy of $\lesssim 5\%$ (Allen et al. 2011).

Joint observations of clusters in SZ, X-ray and optical bands provide multiple mass proxies such as integrated SZ flux, Y_{SZ} (Motl et al. 2005; Nagai 2006); $Y_X = M_{\rm gas}T_X$ (Kravtsov et al. 2006) from X-ray observations; and measurements of velocity dispersions in the optical (Evrard et al. 2008). Forthcoming missions like ASTRO-H would probe the gas motions via X-ray spectroscopy (Inogamov & Sunyaev 2003; Zhuravleva et al. 2012a) and help provide unbiased hydrostatic mass estimates (e.g., Lau, Kravtsov, & Nagai 2009). Such multi-wavelength observations would be useful to check for the consistency of the derived masses and help in identifying the sources of scatter in the mass-observable scaling relations (Battaglia et al. 2012a; Noh & Cohn 2012). Accurate knowledge of this scatter is important for precise determination of the cosmological parameters using cluster surveys (Lima & Hu 2005; Gladders et al. 2007).

In this context, some of the recent efforts have focused on following up many of the SZ detected clusters in X-rays in order to probe the relationship between Y_X and Y_{SZ} (Andersson et al. 2011; Planck Collaboration, et al. 2011b), both of which measure the total thermal energy in the cluster. These works have reported the ratio Y_{SZ}/Y_X at values 0.82 ± 0.07 and 0.95 ± 0.03 respectively, for measurements within a cluster radius of R_{500}[1]. More recently, Rozo et al.

(2012) independently reported this ratio to be 0.82 ± 0.024 using cluster data from Planck and Chandra observations. More data on joint observations of clusters would reduce the statistical and systematic uncertainties and determine the bias between Y_X and Y_{SZ} with better accuracy.

The deprojection analysis of X-ray surface brightness, first implemented for clusters by Fabian et al. (1981), is being routinely performed (in various versions, for e.g., Kriss, Cioffi, & Canizares 1983; McLaughlin 1999; Vikhlinin et al. 2006) to yield the three-dimensional radial profiles of both temperature and density. Henceforth we shall use the term 'deprojection' to imply the particular method as implemented in Churazov et al. (2003) (see also Russell, Sanders, & Fabian 2008). Briefly, assuming spherical symmetry, a set of measured values of the surface brightness in concentric rings is converted into a set of emissivities in spherical shells, using the inverse of a simple geometrical projection matrix. The procedure is repeated for many energies, yielding for each shell an energy dependent volume emissivity - i.e. the spectrum, which is then fitted in XSPEC with the standard model(s).

Thanks to rapid technological progress in SZ observations it has been possible to apply similar methods to well-resolved SZ images obtained with the Planck (Planck Collaboration, et al. 2012), SPT (Plagge et al. 2010), ACT (Reese et al. 2012), CARMA (Plagge et al. 2012), MUSTANG (Korngut et al. 2011) and BOLOCAM (Sayers et al. 2012). From these measurements one may then obtain the volume integrated thermal pressure $\int P dV = \int n_e T dV$, in each concentric shell both in X-rays and SZ, following the deprojection method as outlined in the above paragraph.

X-ray observations reveal the presence of substructures, even in relaxed clusters, with the fluctuations in density and temperature having amplitudes of $\sim 10\%$ (Zhang et al. 2009) at $r \lesssim 0.5 \, R_{500}$ (see also Churazov et al. 2012). Zhuravleva et al. (2012b), henceforth Z12, investigated properties of the ICM fluctuations in simulated clusters and found their distribution to be near-lognormal along with a high density tail contributing $\sim 1\%$ by volume (see also, Roncarelli et al. 2006; Vazza et al. 2011). The width of the density fluctuations is small (0.1 dex) at the centre of relaxed clusters but grows by a factor of 6 at $2 \, R_{500}$; with unrelaxed clusters found to have a broader distribution than relaxed clusters. Z12 propose a simple method for identifying the high density clumps using a sample of simulated clusters and show that the median values of the ICM pressure remain robust to the extraction of such clumps.

If we assume that the X-ray emissivity is independent of temperature[2], and the width of the lognormal distribution of gas density fluctuations, σ_{ne} is small ($\sigma_{ne} \ll 1$), the bias, b_P, between the pressures measured from X-ray (P_X) and SZ (P_{SZ}) observations, as a function of σ_{ne}, in the following three different hypotheses (isothermal, adiabatic and isobaric gas) may be written as,

---

[1] R_{500} is the radius, r, of the cluster within which the enclosed mass, $M(< r)$, equals, $M_{500} \equiv 500\rho_{\rm crit}(z)\frac{4}{3}\pi r^3$; where $\rho_{\rm crit}(z)$ is the critical density of the universe at the observed redshift, z.

[2] The X-ray emissivity in the energy band $E1$–$E2$ is $\epsilon_X \propto n_e^2 \Lambda(E1, E2, T)$. For $T \gtrsim 3$ keV the soft band $(0.5 - 2 \text{ keV})$ emissivity is almost independent of the temperature.
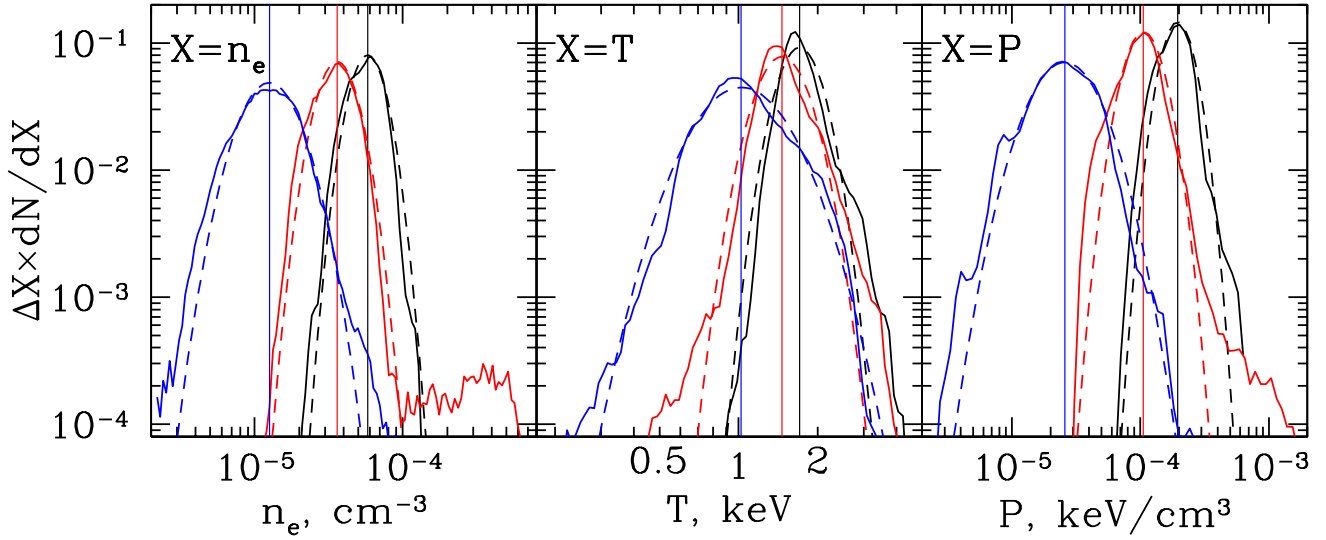
Figure 1. Distribution of density, temperature and pressure in simulated clusters (see Z12, for details). The solid lines show the actual distribution, while the dashed lines indicate the lognormal distribution having the same full width at half maxima. The distributions shown in blue/red/black colours are measured for the (highly relaxed) cluster CL7 in the CSF simulation (see section 3) in concentric shells at the radii, r/R_{500}: 0.9–1.0/1.1–1.2/1.6–1.8. Note the presence of an extended high density tail in the distribution of density fluctuations.

$$b_P \equiv \frac{P_X}{P_{SZ}} - 1 = \frac{\sqrt{\langle n_e^2 \rangle} \langle T \rangle}{\langle n_e T \rangle} - 1 \qquad (1)$$

$$= \exp\left[\frac{\sigma_{ne}^2}{2}\right] - 1 \approx \frac{\sigma_{ne}^2}{2} \qquad \ldots \text{ isothermal}$$

$$= \exp\left[\left(\frac{3}{2} - \gamma\right)\sigma_{ne}^2\right] - 1 \approx -\frac{\sigma_{ne}^2}{6} \quad \ldots \text{ adiabatic}$$

$$= \exp\left[\frac{3\sigma_{ne}^2}{2}\right] - 1 \approx \frac{3}{2}\sigma_{ne}^2 \qquad \ldots \text{ isobaric}$$

for the adiabatic index, $\gamma = 5/3$. It is interesting to note here that the bias takes positive values for isobaric fluctuations but is negative for adiabatic fluctuations.

Thus, for such fluctuations one expects the bias to be simply related to the gas clumping factor, $C \equiv \langle n_e^2 \rangle / \langle n_e \rangle^2 = \exp(\sigma_{ne}^2) \approx 1 + \sigma_{ne}^2$. Note also that the magnitude of this bias is small as long as the fluctuations are not large. Mathiesen et al. (1999) showed using simulations that the average bias in gas mass within R_{500} due to clumpiness in the ICM is about +16%, while Nagai et al. (2007a) found the bias to be lower at $\lesssim$ 6%. Nagai & Lau (2011) showed that clumping may be even larger ($C \sim 2-6$) at the cluster outskirts ($r \gtrsim 1 - 1.5 \ R_{500}$), (see also Vazza et al. 2012).

X-ray and SZ observations provide complimentary information for studying clumpiness and fluctuations in the ICM. However, in reality the actual bias between P_X and P_{SZ} may well be different from the simple estimate presented in equation 1 due to the effects of X-ray instrumental response and, more importantly, the bias resulting from fitting a single temperature model to a spectrum produced by gas with a range of temperatures (e.g. Mazzotta et al. 2004; Kawahara et al. 2007). For example, in a uniform gas having only temperature fluctuations, the measured temperature is weighted down by $\Lambda(E1, E2, T)$ due to the relative

importance of line spectra at lower temperatures, producing a negatively biased P_X with respect to P_{SZ}. In addition, there might also be a bias arising from the application of a simple β model (Rasia et al. 2006) or from the assumption of spherical symmetry for clusters having more complicated morphology (Ameglio et al. 2007), however we shall not discuss these issues here.

It is therefore necessary to make a realistic estimate of the *irreducible* bias between X-ray and SZ measurements of pressure profiles. By irreducible, we mean the bias that would persist even for the most favourable or idealised observations. In this work, we estimate this bias in two ways: (i) From an idealised hot gas described by a lognormal distribution of density and temperature values; (ii) and then from hydrodynamical simulations (with different implementations of input physics) of clusters in a broad mass range. Mock X-ray spectra generated from the given distributions of gas density and temperature are used to estimate this bias. Our computation of this bias takes into account both the density and temperature fluctuations along with their correlation, as well as the effects of the X-ray instrumental response function (for the Chandra telescope) involved in the spectral fitting. We wish to emphasise that in real observations, the bias is likely to depend on the method of deprojection, X-ray instrumental background, ability to remove dense clumps from images (which may be limited by photon statistics), etc. The actual bias inherent in a given X-ray/SZ analysis method should be estimated via detailed tests using the analysis method outlined in section 2 on the mock X-ray observations.

The remainder of the paper is organised as follows: In section 2, we describe the method used to compute the pressure bias from X-ray and SZ observations and apply it to an idealised gas described by a bivariate lognormal distribution of density and temperature fluctuations. In section 3 we

briefly describe the simulations that were used to estimate the bias. In section 4 we discuss the properties of density and temperature fluctuations in the ICM of simulated clusters and define two procedures used to remove the contribution of high density clumpy regions. Next we present the radial profiles of bias in X-ray/SZ pressure measurements along with the biases in the observed densities and temperatures from X-ray observations. In section 5, we compare our results with current and future observations and also with some recent results presented in other theoretical works. Lastly we highlight our main results and conclude.

2   THE BIAS FROM AN IDEALISED HOT GAS WITH A LOGNORMAL DISTRIBUTION

Hydrodynamical simulations of clusters show that the density, n_e, and temperature, T, of the ICM follow a nearly lognormal distribution (Kawahara et al. 2007; Z12) with an extended tail of high density fluctuations (HDF), see Fig. 1. We model an idealised hot gas ($T \sim few$ keV) as a weighted sum of 30×30 components (in densities and temperature) with the weights (here, the emission measures) correctly normalised to follow a bivariate lognormal distribution in n_e and T, defined by the following probability density function,

$$f(n_e, T) = \frac{1}{2\pi n_e T |\mathcal{C}|} \exp\left(-\frac{1}{2}\boldsymbol{X} \cdot \mathcal{C}^{-1} \cdot \boldsymbol{X}^T\right) \quad (2)$$

where, $\mathrm{X} = \left[\ln(n_e) - \mu_{ne} \quad, \quad \ln(T) - \mu_T\right]$

and $\mathcal{C}$ is the covariance matrix,

$$\mathcal{C} = \begin{bmatrix} \sigma_{ne}^2 & \sigma_{ne}\sigma_T\xi \\ \sigma_{ne}\sigma_T\xi & \sigma_T^2 \end{bmatrix}.$$

Such a distribution is characterised by the means of the lognormal distribution, $\mu_{ne} = \langle\ln(n_e/1 \times 10^{-3} \text{ cm}^{-3})\rangle$ and $\mu_T = \langle\ln(T/1 \text{ keV})\rangle$ (or $T_{\text{median}} = \exp(\mu_T)$ keV), the variances, σ_{ne}^2 and σ_T^2, along with the coefficient of correlation, ξ, between $\ln(n_e)$ and $\ln(T)$. Of these, one may always set the density parameter, μ_{ne} to an arbitrary value since we are only interested in computing the ratio P_X/P_{SZ}; henceforth we shall not mention the value of this parameter.

2.1   Method: Mock X-ray spectrum

We use the MEKAL code in XSPEC (Mewe et al. 1985, 1986; Kaastra 1992; Liedahl et al. 1995) to generate the X-ray model spectra from a hot diffuse gas, including the line emissions from the astrophysically abundant elements, for each of the components defined by the values of n_e and T. The choice of the MEKAL model was motivated by its ability to calculate anew the spectrum at any given temperature, rather than interpolate from tabulated values as in the APEC model[3]. These spectra are then added together to produce a composite spectrum of X-ray emission from an ICM having a distribution of temperatures and densities.
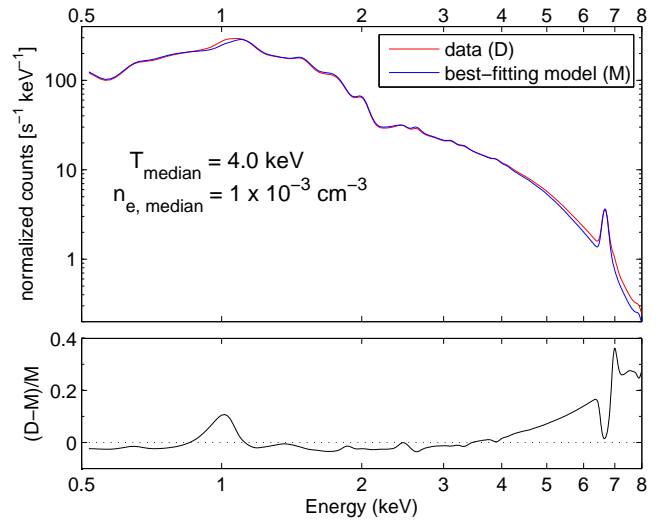
Figure 2. Single temperature fit to a composite spectrum, for the Chandra response. *Upper panel:* The red curve shows the composite spectrum generated from a bivariate lognormal distribution of gas components with $\sigma_T = 0.45$, $\sigma_{ne} = 0.55$ and correlation $\xi = -0.55$, while the blue curve is the best-fitting single temperature MEKAL spectrum. *Lower panel:* Difference between the data and model. For this spectrum the best-fitting values of density and temperature are 1.38×10^{-3} cm^{-3} and 3.91 keV, giving biases of +16.8% and -23.3% w.r.t. $n_{\text{ref}} = 1.16 \times 10^{-3}$ cm^{-3} and $T_{\text{ref}} = 3.91$ keV respectively (see equation 3). Using equation 4, the bias in pressures turns out to be -10.4%. A metallicity value of 0.35 was assumed relative to the solar abundance (Anders & Grevesse 1989).

This composite spectrum is next fitted by a single component MEKAL model (in the energy range 0.5 - 8.0 keV) to obtain the best-fitting values $n_{e,\text{fit}}$ and T_{fit} using the Chandra instrumental response file. The X-ray electron pressure, $P_X = n_{e,\text{fit}}T_{\text{fit}}$, for the ICM is then computed from these best-fitting values of density and temperature[4].

The bias in the gas density is defined with respect to the volume-weighted density and the bias in temperature is defined with respect to the mass weighted temperature,

$$n_{\text{ref}} = \frac{\int n_e dV}{\int dV} \quad ; \quad T_{\text{ref}} = \frac{\int T n_e dV}{\int n_e dV}. \quad (3)$$

With these definitions the SZ pressure is, $P_{SZ} = P_{\text{mean}} = n_{\text{ref}}T_{\text{ref}}$ and the bias in pressure may be written as,

$$b_P \equiv \frac{P_X}{P_{SZ}} - 1 = \frac{n_{e,\text{fit}}}{n_{e,\text{ref}}} \frac{T_{\text{fit}}}{T_{\text{ref}}} - 1. \quad (4)$$

The top panel of Fig. 2 shows the mock X-ray spectrum generated from a hot diffuse gas that has a bivariate lognormal distribution (red line) with a median temperature, $T_{\text{median}} = 4$ keV and median density, $n_{e,\text{median}} = 1 \times 10^{-3}$ cm^{-3}. The blue line shows the best-fitting spectrum specified by a single value of temperature and density. Using equation 4 we compute the pressure bias, $b_P = -10.4\%$.

---

[3] We find that the APEC model (Smith et al. 2001) produces small spurious jumps in the bias caused by the interpolation of the tabulated spectra. These jumps are absent in the MEKAL model if the emission spectra are calculated anew for each model.

[4] Note that when fitting a MEKAL model to the composite spectrum we allow only the temperature and normalisation to be free parameters, while the redshift, metal abundances, and the Hydrogen column density are kept fixed.
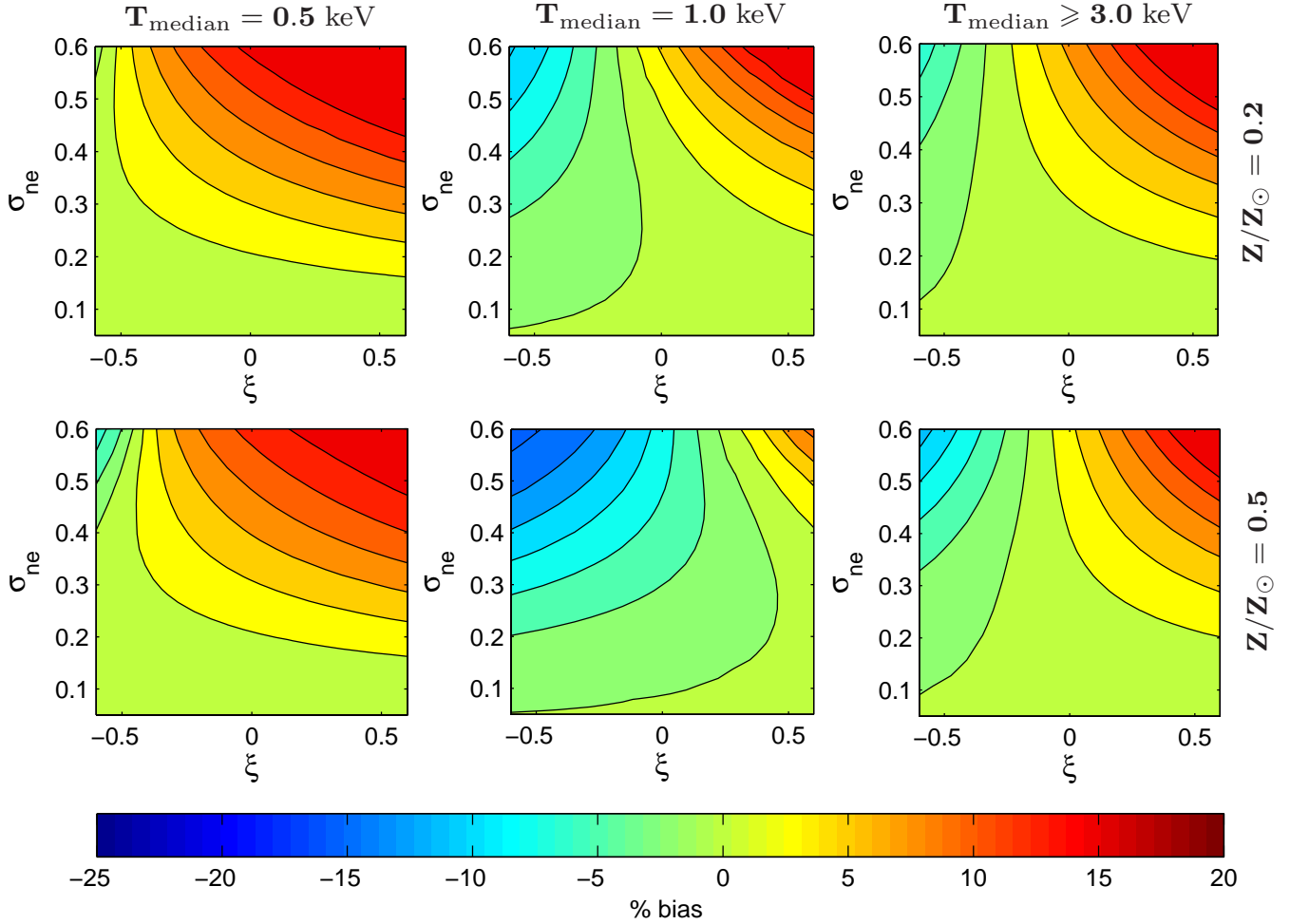
Figure 3. Contour map predicting the bias, $b_P \equiv P_X/P_{SZ} - 1$, for an idealised hot gas described by a bivariate lognormal distribution of density and temperature fluctuations for various values of median temperatures, T_{median} (in columns) and assumed metallicities (in rows). The bias values are indicated on the colourbar (in percentage) as a function of two parameters σ_{ne} and ξ, using the best fitting relation from Fig. 5, $\sigma_T = 0.73\sigma_T - 0.02$. The green contours indicate the zero bias, while adjacent contours are in increments of 2.5%. At higher values of T_{median}, the dependence of bias on ξ and σ_{ne} is very similar to that indicated by $T_{\mathrm{median}} = 3$ keV. The bias has been computed by fitting a single temperature spectrum in the energy band 0.5–8.0 keV and using the Chandra response function.

2.2 Results: Bias from a lognormal distribution of gas density and temperature fluctuations

As a preliminary check we verified that our scheme reproduces the simple estimate of the ratio $P_X/P_{SZ} = n_{e,\mathrm{fit}}/n_{e,\mathrm{ref}} = \sqrt{C}$ when the temperature fluctuations are set to zero, while retaining only the density perturbations (see also equation 1). This is done by generating a mock spectrum from a lognormal distribution of density fluctuations, convolving it with the instrument response (Chandra response in our case) and then fitting it to a single temperature model, as explained before in section 2.1, to compute the bias using equation 4. We then go on to systematically explore the dependence of bias in an idealised hot gas described by a bivariate lognormal distribution of density and temperature fluctuations (see equation 2). For this we compute the bias (as described in section 2.1) as a function of the parameters $\{\sigma_T, \sigma_{ne}, \xi, T_{\mathrm{median}}\}$ for values in the range – $0.01 \leqslant \sigma_T, \ \sigma_{ne} \leqslant 0.6$, and $-0.6 \leqslant \xi \leqslant 0.6$ at various temperatures, $T_{\mathrm{median}} \geqslant 0.5$ keV,

for an assumed value of metallicity. We find that the bias is most sensitive to the value of ξ, the coefficient of correlation between density and temperature fluctuations (see equation 2). Keeping the other parameters fixed, the bias always increases almost linearly with ξ for $|\xi| < 0.55$. The rate of increase however depends on the widths of the distribution of temperature and density fluctuations, i.e. σ_T and σ_{ne}. The simple linear dependence of the bias on ξ implies the possibility of probing the nature of perturbations in the ICM: $\xi < 0$ would indicate the relative importance of isobaric or entropy[5] perturbations, while $\xi > 0$ would imply that adiabatic or pressure perturbations (caused by sound waves or weak shocks) are dominant.

We now try to describe the dependence of the bias in pressure in terms of the parameters of the bivariate lognormal distribution using a fitting form. For values of the

---

[5] Here entropy is defined as $S \equiv k_B T/n_e^{2/3}$, where n_e and T are electron density and temperature of the ICM respectively.

Table 1. Values of the best-fit parameters of the fitting form in equation 5 to predict the bias, $b_P \equiv P_X/P_{SZ} - 1$, in X-ray vs SZ pressure, valid at temperatures, $T_{\mathrm{median}} \geqslant 3$ keV.

$Z/Z_\odot$	p_1	p_2	p_3
0.20	0.69	0.75	1.48
0.35	0.75	0.83	1.31
0.50	0.80	0.99	1.08

median gas temperature, $T_{\mathrm{median}} \geqslant 3$ keV, the bias may be parametrised using three free parameters as follows,

$$b_P = \frac{1}{2}\sigma_{ne}^2 - p_1\sigma_T^2 + p_2\ln(1 + p_3\sigma_T)\sigma_{ne}\xi. \qquad (5)$$

The best-fitting values of the parameters are indicated in Table 1 for a range of assumed metallicites. This fitting formula is accurate (in absolute terms) to within 0.01 for $\sigma_{ne/T} \leqslant 0.3$ with $|\xi| \leqslant 0.6$ and within 0.05 for $\sigma_{ne/T} \leqslant 0.6$ with the same range for ξ. We verified that these conditions hold for the ICM within R_{500}, in simulated clusters (see Section 4.3 and the discussion on Fig. 7). For median temperatures greater than 3 keV, the X-ray emissivity in the 0.5–8 keV band is only a weak function of temperature; at lower temperatures however, there is a significant dependence due to relative importance of discrete spectral line emission, causing the measured bias to depart significantly from this parametrisation. We find that a decrease in the median temperature below ~ 1 keV causes the bias to change steeply in a nontrivial manner, which is difficult to parametrise through a simple form.

In general the bias in pressure for an assumed value of metal abundances depends on 4 parameters – σ_T, σ_{ne}, ξ and T_{median}. However, we may simplify this by eliminating a parameter using an approximate relation, $\sigma_T = 0.73\sigma_T - 0.02$, that is seen in hydrodynamical simulations of clusters (see Fig. 5). With this simplification, in Fig. 3 we plot the bias contours for various values of median temperatures as a function of ξ and σ_{ne} assuming two values of gas metallicities, $Z/Z_\odot = 0.2$ and 0.5; the former being the typical value beyond 0.2 R_{180}, while the latter is indicative of the ICM metallicities at the centre of the cluster (e.g. Leccardi & Molendi 2008). We see that for ICM temperatures, $T_{\mathrm{median}} > 3$ keV, the bias is small (from -10% to $+5\%$) for most of the parameter space in the (ξ, σ_{ne}) plane. Only for higher values of both the fluctuations and the negative correlation ξ, the bias goes beyond -15%. For lower temperatures (1 keV $< T_{\mathrm{median}} < 3$ keV), this bias can be between -25% to $+15\%$, depending on the metal abundance; while for even lower temperatures the bias turns positive, mostly lying at the $0 - 10\%$ level. Note that especially for low temperatures ($T_{\mathrm{median}} < 3$ keV) the value of bias is more sensitive to the assumed metal abundance; the effect of increasing metallicity is to reduce the bias when positive, or to move it towards more negative values otherwise.

3   SIMULATIONS AND SAMPLE OF GALAXY CLUSTERS

We use a sample of 16 simulated clusters at $z = 0$ taken from Nagai et al. (2007a,b). The simulations were done using the Adaptive Refinement Tree (ART) N-body+gas-

Table 2. Properties of simulated clusters in the sample of Nagai et al. (2007a,b) at $z = 0$. Two runs were performed with different physics, CSF run with cooling+star formation and NR run without radiative cooling and star formation. The last column indicates if the cluster is visually identified as relaxed (R) or unrelaxed (U).

Cluster ID	R_{500} (h^{-1} Mpc)	M_{500}^{tot} (10^{14} h^{-1} M$_\odot$)	Relaxed (R) or Unrelaxed (U)
	CSF / NR	CSF / NR	CSF / NR
CL101	1.16 / 1.14	9.08 / 8.62	U / U
CL102	0.98 / 0.95	5.45 / 4.63	U / U
CL103	0.99 / 0.99	5.71 / 5.71	U / U
CL104	0.97 / 0.97	5.39 / 5.31	R / R
CL105	0.94 / 0.92	4.86 / 4.50	U / U
CL106	0.84 / 0.84	3.47 / 3.40	U / U
CL107	0.76 / 0.78	2.57 / 2.74	U / U
CL3	0.71 / 0.70	2.09 / 1.98	R / R
CL5	0.61 / 0.61	1.31 / 1.34	R / U
CL6	0.66 / 0.61	1.68 / 1.32	U / R
CL7	0.62 / 0.60	1.41 / 1.25	R / R
CL9	0.52 / 0.51	0.823 / 0.775	U / U
CL10	0.49 / 0.47	0.672 / 0.621	R / R
CL11	0.54 / 0.44	0.899 / 0.482	U / R
CL14	0.51 / 0.48	0.769 / 0.652	R / R
CL24	0.39 / 0.39	0.347 / 0.347	U / U

dynamics code (Kravtsov et al. 1997, 2002) assuming a flat ΛCDM cosmology with the following values for the cosmological parameters: $\Omega_m = 0.3, \Omega_b = 0.04286, h = 0.7$ and $\sigma_8 = 0.9$. Two types of simulations were used with different physics involved, but with the same initial conditions: (i) non-radiative (NR) runs without any radiative cooling and (ii) cooling plus star formation (CSF) runs, which included metallicity-dependent radiative cooling, star formation, supernova feedback and UV background. The clusters in the sample were selected randomly to uniformly sample the mass range, 7×10^{13} h^{-1} M$_\odot$ $< M_{500} < 2\times10^{15}$ h^{-1} M$_\odot$. These clusters were selected from low-resolution simulations and resimulated at a higher resolution. The division of the sample into relaxed and unrelaxed sub-samples (see Table 2) was done in Nagai et al. (2007a) by visually examining the morphology of mock X-ray images in three different projections. This was done by producing mock images of the simulated clusters using the Chandra response function with a 100 ks exposure. From these images the 'relaxed' clusters were identified as those with a regular X-ray morphology and without any significant deviations from elliptical symmetry. On the other hand, clusters were classified as 'unrelaxed' when departures from elliptical symmetry, filamentary X-ray structures, or large isophotal centroid shifts were seen in the produced images. This procedure is similar to that used by observers. Z12 made another classification based on the widths of the density distribution, σ_{ne}, at $r = R_{500}$. This classification agrees very well with that done in Nagai et al. (2007a), and the difference in $\sigma_{ne}(R_{500})$ between relaxed and unrelaxed clusters was at the level of $\simeq 2.5\sigma$. There also exist other schemes of classification, for e.g. using the two dimensional multipole expansion of the projected gravitational potential (Buote & Tsai 1995) or computing the centroid shifts (Poole et al. 2006); however we did not compare our classification with these.

The ART code uses a non-uniform and dynamic mesh

adjusting to the evolving particle distribution, thus allowing for a large dynamic range. To simplify our analysis, the code output (gas densities, temperatures, velocities, and metallicities) was interpolated onto a uniform grid with grid cells of size comparable to the effective resolution of the cluster simulations. Following Z12, we randomly sample 4×10^7 data points within the sphere of radius of 5 h^{-1} Mpc with a weight $\propto 1/r^2$, where r is the distance from the cluster centre. This sampling is uniform in azimuthal and polar directions and provides equal number of points per spherical shell of a given thickness. Such a scheme is useful for dealing with averaged quantities computed over spherical shells as discussed further in the following sections.

4   THE BIAS FROM SIMULATED GALAXY CLUSTERS

In this section we shall compute the bias between 'measured' pressure profiles from X-ray and SZ observations using the sample of simulated clusters introduced in the previous section. We wish to emphasise that the term 'measured' (here and henceforth) refers to the value of pressure as would be inferred from observations in X-ray/SZ through a deprojection analysis of real data. Note that this may well be different from the actual values of thermal pressure of the ICM.

Each cluster is divided into 32 concentric shells (spaced in equal logarithmic intervals) between the radii $0.1 < r/R_{500} < 2.3$, in which we compute the histogram of density and temperature values. This is then used to generate fake spectra assuming[6] a metallicity of $Z/Z_{\odot} = 0.35$, as described before in section 2.1. The fake spectra are then analysed using the Chandra response matrix to give the best-fitting values of density, $n_{e,\mathrm{fit}}$ and temperature, T_{fit} for each shell. The 'measured' X-ray pressure is then simply $P_X = n_{e,\mathrm{fit}} T_{\mathrm{fit}}$. On the other hand the SZ pressure for each shell is obtained by computing the mean thermal pressure in the shell $P_{SZ} = \sum_i n_{e,i} T_i w_i / \sum_i w_i$, where w_i is the weight, i.e. the fractional volume occupied by the ICM specified by the values $n_{e,i}$ and T_i for density and temperature respectively. These are used now to compute the bias, $b_P(r) = P_X(r)/P_{SZ} - 1$ between the 'measured' X-ray and SZ pressures, in each shell.

4.1   Properties of the ICM fluctuations

Z12 used the same set of simulations, as described in section 3, to study the properties of the inhomogeneities in the ICM. They developed a simple and robust method to separate the HDF from the nearly hydrostatic bulk component. This was implemented by imposing a cut within each shell to exclude all particles having densities, n_e, such that $\log(n_e) > \log(n_{e,\mathrm{median}}) + 3.5\sigma_{ne}$. Henceforth we shall use

---

---

the term 'HDF' to exclusively denote the particles in the simulation lying above this cut, and the term 'bulk' to describe the particles lying within this cut.

Here we review some of the results presented in Z12. Fig. 4 shows the radial profiles indicating the properties of ICM fluctuations for the sample of relaxed clusters in the NR simulations. In Fig. 4 (a) the solid lines denote the median values (over the sample of relaxed clusters in the NR run) of the parameters obtained by fitting a bivariate lognormal distribution (see equation 2) within each shell. The dashed lines are the same quantities computed *after* the removal of the HDF components. The thin lines indicate the maximum and minimum outliers of the sample that shows the scatter across the sample. Fig. 5 shows the relation between the parameters σ_{ne} and σ_T in each shell; the straight line is the best-fitting linear relation, $\sigma_T = 0.73\sigma_{ne} - 0.02$, which is also the assumption used in producing the contours in Fig. 3. The data from NR and CSF simulations indicate an intrinsic scatter of 0.07 in σ_T for a given value of σ_{ne} in this relation. Fig. 4 (a) and (b) show that the values of the parameters, σ_{ne} and ξ, are fairly robust to the exclusion of the HDF components from the bulk.

In both the CSF and NR runs, the unrelaxed clusters have not only higher values of temperature and density fluctuations, but also show significantly larger scatter from cluster to cluster. Both relaxed and unrelaxed clusters show a steady increase in the fluctuation amplitude with radius, which steepens in the outskirts ($r > R_{500}$). As shown in Fig. 4 (a), the fluctuations in gas density, σ_{ne}, are large beyond R_{500}, and these fluctuations are reduced if the HDF components are removed. Fig. 4 (b) shows that the correlation between temperature and density fluctuations, ξ, is mostly negative, but increases towards zero at larger radii. The increase in ξ on removal of high density clumps is in line with our expectations, as the clumpy regions contribute to an anti-correlation (or $\xi < 0$) between density and temperature fluctuations.

4.2   Removing the contribution from the brightest clumpy regions in the cluster outskirts

We expect the 'measured' quantities related to the ICM (e.g., gas pressure, density and temperature) to be less biased when the HDF components are removed from the simulation data. Clearly the removal of HDF according to the criterion described in the previous section is only possible in simulations. In real observations, the complete removal of HDF seems unlikely, due to the presence of the X-ray background noise and limited photon statistics, especially relevant at the cluster outskirts or for the high redshift clusters. Here we shall attempt to check this by dealing directly with the 2-dimensional projected X-ray images obtained from the simulated clusters, only in the limit of infinite photon statistics (i.e., without any Poisson noise) and in the absence of instrumental background. However, we shall argue in section 4.3 that even a partial removal of the clumps, especially the brightest ones (as permitted by the photon statistics), helps to reduce the bias to a large extent.

For each of the clusters, we divide the X-ray images into six radially equal annular regions starting from $r = R_{500}$ as the innermost ring and up to $r = 2.3\,R_{500}$. We choose R_{500} as the inner radius for the purpose of remov-
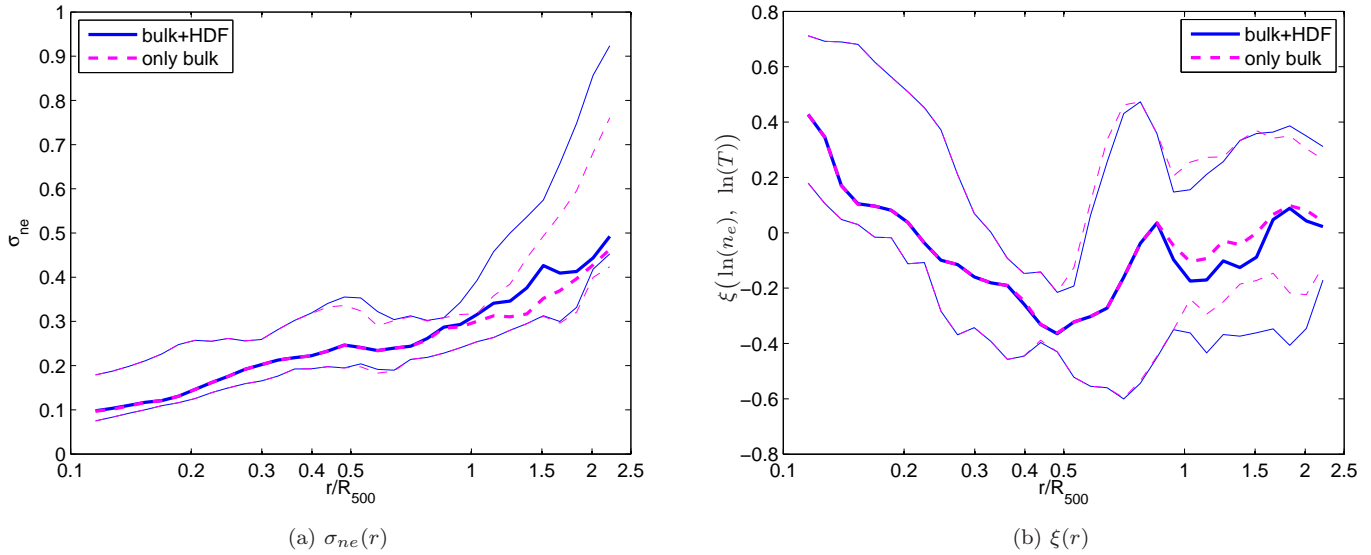
(a) $\sigma_{ne}(r)$ (b) $\xi(r)$

Figure 4. Radial profiles showing the rms of fluctuations in density, σ_{ne} (characterised by a lognormal distribution), for a sample of relaxed clusters in the NR simulations. The thick lines indicate the sample median while the thin lines denote the sample outliers. The solid and dashed lines correspond to the ICM with and without high density fluctuations (HDF), respectively.
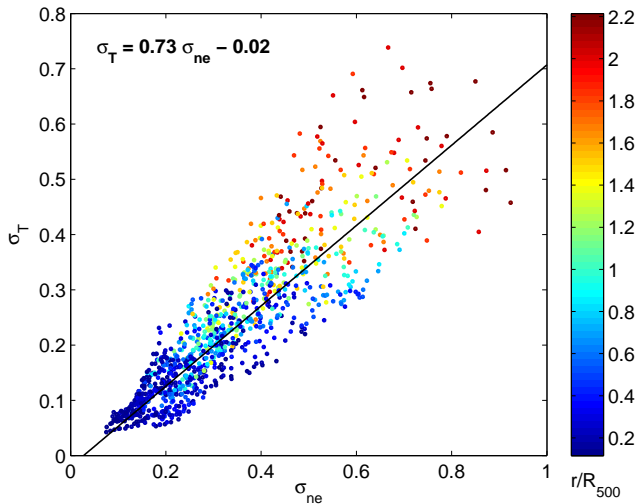

Figure 5. The coloured dots indicate the values of fluctuations in density, σ_{ne}, and temperature, σ_T, in concentric shells from the combined sample of clusters in both the NR and CSF simulations. The colours (mapped to colourbar on right) indicate the radial distance of the shell from the cluster centre. The black line indicates the best fitting linear relation, $\sigma_T = 0.73\sigma_{ne} - 0.02$. For this relation the scatter in σ_T for a given value of σ_{ne} is 0.07.

ing clumps since we find that the bias outliers become large only beyond this radius, suggesting that the effect of clumps is dominant in the bias profiles only in the outskirts ($r > R_{500}$) of clusters (see also Mathiesen et al. 1999; Nagai & Lau 2011; Battaglia et al. 2012b; Vazza et al. 2012, and Fig. 7). Using the pixels lying within each annular region we then create histograms of the X-ray brightness (in the soft band from 0.5-2.0 keV using the Chandra response) and mask all pixels with brightness, B, such that

$\log(B) > \log(B_{\rm median}) + f_{\rm cut}\sigma_B$, to zero values, where σ_B is the standard deviation of the logarithm of pixel brightness in each annulus. Using three different values of $f_{\rm cut}$ — 2, 2.5 and 3, we then eliminate all the particles from the simulation data which lie exactly along the line of sight of the masked pixels, some of which are responsible for producing the very bright regions in the outskirts of the X-ray image. We shall henceforth refer to this method of removing the high-density contributions from the X-ray images as the 2-D cut in contrast with the 3-D cut performed directly on the radial shells and as outlined in section 4.1 and detailed in section 4 of Z12.

We note that the 2-D cuts do not remove all of the clumpy contributions from the 3-dimensional radial shells, partly because clumps lying along the line of sight through the bright central region of the projected image of the cluster would not show up with high enough contrast in the brightness images, and would remain in the filtered (i.e. after a 2-D cut) simulation data. For a fair comparison of the results from 2-D cut and 3-D cut we attempt to correct this by applying a projection in another plane and repeating the masking procedure in this new plane. Fig. 6 shows a comparison of projected X-ray images of the simulated cluster CL101 under 2-D (using $f_{\rm cut} = 2.5$) and 3-D cuts. On the left is the original image produced without any cuts, while the central and the rightmost images are after application of 3-D and 2-D cuts respectively. Note that the 3-D cut is applied everywhere while the 2-D cut is only applied within $R_{500} < r < 2.3\ R_{500}$ (indicated by the annulus which is bounded by green circles). We see that the bright clumps in this annulus, visible prominently on the leftmost image are absent after applying either the 3-D or 2-D cuts. The fact that this annulus appears very similar after 2-D and 3-D cuts indicates that both of these cuts remove nearly the same points from the 3-D shells.

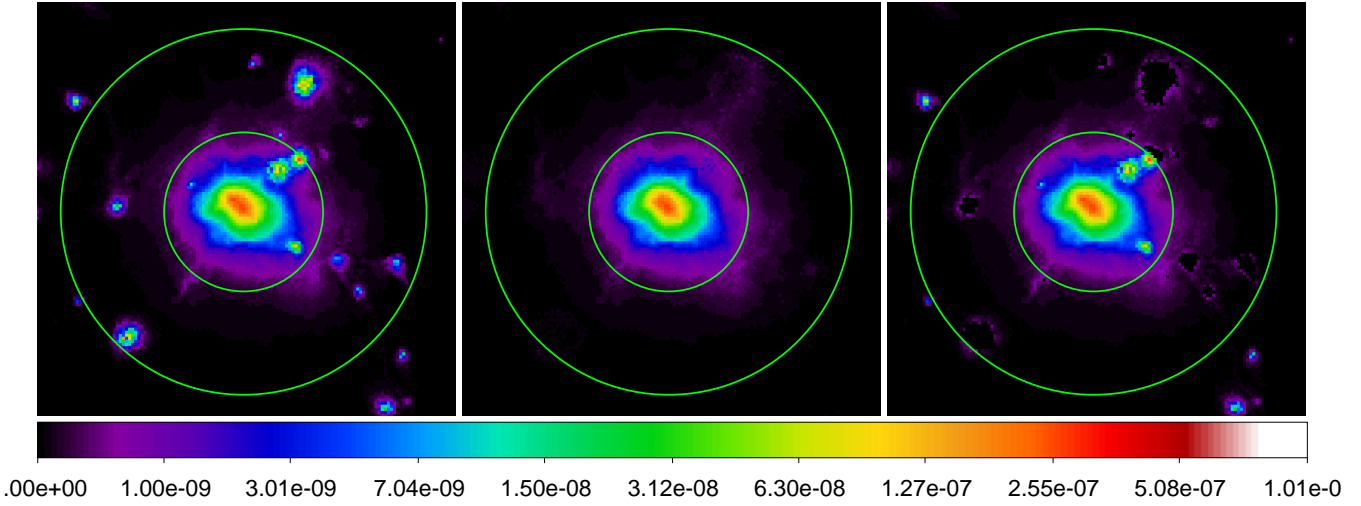We now try to examine if a similar 2-D cut (or mask-

| .00e+00 | 1.00e-09 | 3.01e-09 | 7.04e-09 | 1.50e-08 | 3.12e-08 | 6.30e-08 | 1.27e-07 | 2.55e-07 | 5.08e-07 | 1.01e-0 |

Figure 6. Exclusion of the bright clumps from the projected soft band (0.5–2.0 keV) X-ray image of the simulated cluster CL101 in the NR run. The images from left to right are: (i) Original image; (ii) Image showing only the bulk component (i.e. with 3-D cut); (iii) Image after masking of the brightest regions (i.e. with 2-D cut specified by the value $f_{\rm cut} = 2.5$). The 2-D mask is applied in the region $R_{500} < r < 2.3\, R_{500}$ whose boundaries are indicated by the green circles, while the 3-D mask is applied everywhere.

ing) is possible in real observations, where the ability to mask the clumps would depend on the signal to noise ratio at $r \gtrsim R_{500}$. To be able to identify and mask such regions it is necessary that the intrinsic fluctuations of surface brightness should dominate over the Poisson fluctuations of the photon counts. We now estimate the minimum number of counts required in order to be able to mask such clumps, provided that they are resolved by the instrument. Let N be the total number of counts, $n_{\rm reg}$ be the number of independent regions (or pixels used for masking); then, we have $n = N/n_{\rm reg}$ as the number of counts per region. To reliably remove the region with the surface brightness X times the mean value (i.e. Xn counts) one needs (case with no background) as a conservative estimate: $(X - 1)n > 5\sqrt{n}$ for $n \gg 1$, or $(X - 1)n > 5$ for $n \ll 1$. For the case shown in Fig. 6 we use 63 by 63 kpc pixels, yielding $N_{\rm reg} = 9048$ in the annulus from R_{500} to $2.3\, R_{500}$. Assuming 100,000 counts for the whole image, and 7.0% flux coming from this annulus, the typical number of counts per pixel, $N/n_{\rm reg} = 0.78$. Thus, pixels with the surface brightness $X > 6.4$ are easily detectable as more than 5σ deviations on top of the mean level. To get 100,000 photons in the 0.5–2.0 keV band the Chandra ACIS-I instrument with an effective area[7] of $\sim$370 cm^2 would require an exposure time of $\sim$10 ks for the simulated cluster CL101 with a mass of $\sim 1.2 \times 10^{15}$ M$_\odot$ and $\sim$150 ks for CL24 with a mass of $\sim 5.0 \times 10^{13}$ M$_\odot$, assuming a redshift of $z = 0.1$ for both objects. Further, we see that the clumps in the image will still be resolved if the size of the pixels is increased by a factor of ~ 2.5. This reduces the required number of photons, we now find that pixels with surface brightness $X > 10.25$ can be used for masking, using

$f_{\rm cut} = 2.5$ and 3.0, even if there are 10,000 counts for the whole image.

4.3 Results: Bias between X-ray and SZ pressure profiles

Fig. 7(a) shows the median bias profile of the relaxed clusters in the NR run. The profiles with and without HDF components (the 3-D cut) are shown by the thick solid blue and thick dashed magenta lines, respectively. Thick dot-dashed black line shows the median profile with the exclusion of the bright clumps beyond R_{500} in the projected map (the 2-D cut with $f_{\rm cut} = 2.5$). The sample outliers are indicated by the thin lines of similar type. Note that this bias is computed from the composite spectra corresponding to the actual distribution of temperature and density values within each shell (see section 2.1), and not from the idealised log-normal distribution. We find the median bias computed from the relaxed clusters to be within 0% to +2% at $r < 0.5\, R_{500}$. This then decreases to negative values $\sim -6\%$ at $r = R_{500}$. The bias profiles remain unaffected by the HDF component (due to small fluctuations) within R_{500}, producing almost identical profiles with and without HDF. Beyond R_{500}, the median bias profiles from 'only bulk' follow the same trend as 'bulk+HDF', but are smoother and are limited to within -2.5% to $+2\%$. With the 2-D cuts, the median bias profile is also smoother and agrees with the bias profile after the 3-D cut (see the lower panel of Fig. 8).

We find that the unrelaxed clusters display a larger negative bias and larger scatter, both from shell to shell and across the sample at a given value of r/R_{500}. The cluster-to-cluster scatter increases with radius. At $r = R_{500}$, the scatter is less than 3% and 13% for relaxed and unrelaxed clusters, respectively, for the NR run. At larger radii ($r \sim 2\, R_{500}$), the scatter is highly skewed in the positive direction, with some shells showing $b_P \gg 0$ (see Fig. 8), from the presence of dense clumps. After the 3-D cut, the scatter in the pressure
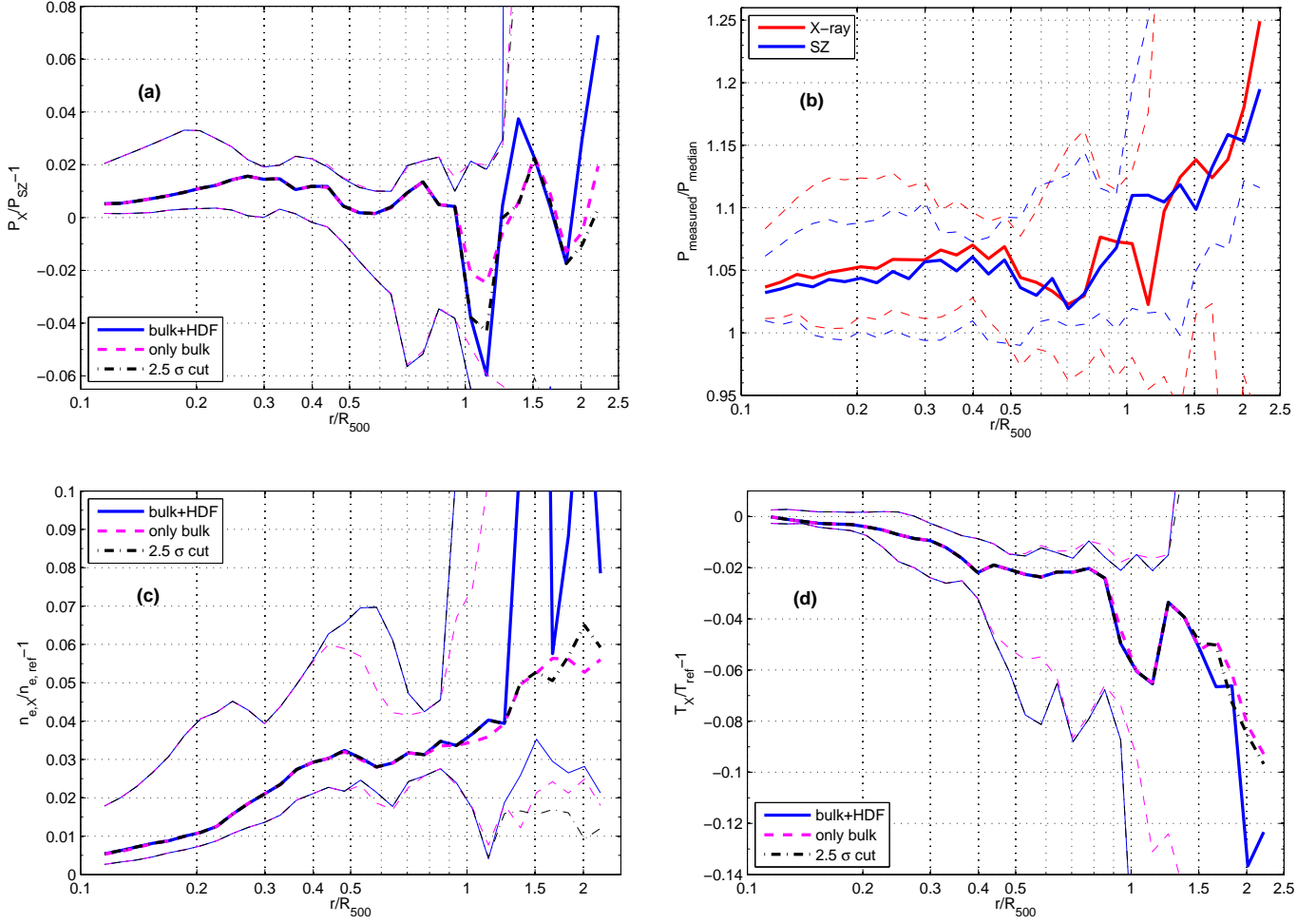
---

[7] This is the weighted average effective area over the energy range 0.5–2.0 keV for a hot gas with $T \sim few$ keV. The photon rate used to estimate the exposure was also computed for the same energy range.

Figure 7. Radial profiles showing various biases computed in concentric radial shells of a sample of relaxed clusters in the non-radiative simulations. In all the figures, the thick lines indicate the median profile while the thin lines are the most extreme outliers in the sample.
(a) Pressure bias, $b_P \equiv P_X/P_{SZ} - 1$, for the 'measured' X-ray (P_X) and SZ (P_{SZ}) pressures.
(b) The ratio of the 'measured' X-ray/SZ pressures to the median pressure shown in thick red/blue lines for 'bulk+HDF'.
(c) Bias in the 'measured' density from X-ray observations with respect to n_{ref} (see equation 3).
(d) Bias in the 'measured' temperature with respect to the mass weighted temperature, T_{ref} (see equation 3). The 'measured' temperature is determined simultaneously with the best-fitting n_e.

bias drops to less than 7% within R_{500} even in unrelaxed clusters.

Fig. 7(b) shows the 'measured' values of the X-ray and SZ pressures w.r.t. the *median* pressure in concentric shells at various radii. Since the value of P_{SZ} actually corresponds to the average electron pressure, the fact that there is a bias even in the SZ profiles implies that the mean and the median values of pressure fluctuations are different. This is true for any asymmetric distribution such as the near-lognormal distribution of pressure fluctuations seen in Fig. 1. The plot shows that the 'measured' SZ and X-ray pressures are largely similar, the differences between them are smaller than differences in the mean and median values of pressure fluctuations.

In Fig. 7(c) and (d), we also plot the bias in the density and spectroscopic temperature values as would be 'measured' from X-ray observations. As seen from equation 1

the best-fitting values of n_e are biased in the positive direction, while the best-fitting T_X is biased negatively. For the relaxed clusters in the NR simulation, the median bias in gas density increases slowly to +3.5% at R_{500} but can reach $\sim +40\%$ at larger radii. Interestingly, the exclusion of bright clumps reduces the median bias to +6.5% at $r = 2\,R_{500}$ and makes the bias profile considerably smoother. Beyond R_{500} the median bias profiles in gas density obtained after both 3-D and 2-D cuts are quite similar. The median bias in temperature takes similar values up to $r \sim 0.8\,R_{500}$ as the density bias, but in the negative direction, reaching $\sim -14\%$ at $r = 2\,R_{500}$. We find that the median bias in temperature reduces only slightly even after removing the HDF, because the removal of the HDF components only affects the density distribution, but does not directly limit the temperature fluctuations. This is because, there is almost zero correlation between density and temperature fluctuations (see Fig. 4

(b)) in the ICM at $r > R_{500}$. At the same time, the sample outliers producing a negative bias in temperature reduce to nearly a third of the original value after the 2-D and 3-D cuts (as the very dense clumps are cold).

In Fig. 8 we compare the bias profiles in pressure, in the cluster outskirts ($r > R_{500}$), for the various cuts in surface brightness applied in concentric annuli on the projected images of the NR simulations. We also plot for comparison the results from the 'HDF+bulk' (No cut) and 'only bulk' (3-D cut). We find that application of more stringent cuts (specified by lower values of f_{cut}) reduces the scatter in the bias profiles. Exclusion of the bright clumps in the cluster outskirts ($r > R_{500}$) reduces the outliers (on the positive side) in the bias (b_P) profiles, by more than an order of magnitude, from +8.2 to +1.8, +1.2, and +0.7 respectively, at 2.2 R_{500}, for $f_{cut} = 3.0$, 2.5 and 2.0. For $f_{cut} = 2.0$ the excluded clumps have surface brightness between ~ 9 – 13 times that of the average value (across the inner to the outer annuli). For $f_{cut} = 2.5$ this is 13–18; while for $f_{cut} = 3.0$ these numbers are 20–28. It is clear that such exclusions would remove only the brightest regions associated with high density clumps, as shown in Fig. 6 for the unrelaxed cluster CL101 in the NR run. On the negative side (i.e. outliers with $b_P < 0$), the various cuts do not affect the outliers as much as for the positive side. We see from the bias profiles plotted in the upper panel of Fig. 8 that the 2-D cut specified by the value $f_{cut} = 2.5$ produces similar results to the 3-D cut. A more stringent cut ($f_{cut} = 2.0$) may further eliminate the intrinsic brightness fluctuations associated with inhomogeneities in the diffuse ICM, while a more relaxed cut ($f_{cut} = 3.0$) does not remove all the visibly bright clumps. In the lower panel of Fig. 8 we indicate the median values of the bias for the 16 clusters; these are again quite robust to the application of the various 2-D and 3-D cuts.

Finally, we compare the bias in the median pressure profiles, $b_P \equiv P_X/P_{SZ} - 1$, for both relaxed and unrelaxed clusters in simulations with very different input physics. As expected, we find more clumping in the CSF simulations when compared to the NR simulations; the bias profiles in the CSF runs also display significantly larger scatter from shell to shell (over the same radial range) due to the presence of some very dense clumps. Fig. 9 shows the median bias profiles to be within -4% to $+2\%$ for $r < 0.5$ R_{500} and within -6% to $+2\%$ for 0.5 $R_{500} < r < R_{500}$ for relaxed and unrelaxed clusters in both NR and CSF simulations. At $r \approx 1.2$ R_{500}, the bias reaches -13%, arising from the presence of infalling clumps, but reduces to less than -5% when the HDF component is removed. In both the NR and CSF simulations the bias increases beyond $r \gtrsim 2$ R_{500}.

More importantly, we find that the pressure bias is limited to within $\pm 15\%$ for any of the relaxed simulated clusters in both CSF and NR runs of the simulation inside R_{500}. Also, the results on median bias profiles are quite similar (see Fig. 9) across very different input physics used in the NR and CSF runs. This suggests that our results are robust to possible uncertainties in the implementation of physical processes in the hydro codes.
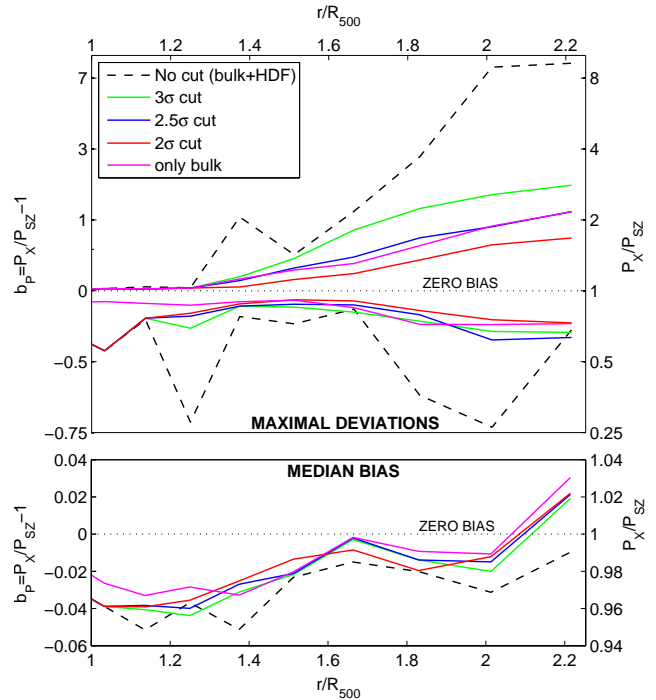
Figure 8. Reduction of the bias, $b_P \equiv P_X/P_{SZ} - 1$, in the pressure profiles by the introduction of various cuts in surface brightness (applied to the X-ray images), at $r \geqslant R_{500}$. *Upper panel:* Maximal deviations (or sample outliers) for both relaxed and unrelaxed clusters in the NR simulation. *Lower panel:* Median bias profiles for each of the above cuts. Note that in both panels, the left axis shows $b_P = P_X/P_{SZ} - 1$ while the right axis displays P_X/P_{SZ}; the dotted line, 'ZERO BIAS' indicates $b_P = 0$ or $P_X/P_{SZ} = 1$.

5   COMPARISON WITH CURRENT AND FUTURE MEASUREMENTS

High-resolution observations of galaxy clusters jointly in X-rays and millimetre/sub-millimetre bands provide independent measures of the thermal pressure profiles through a deprojection analysis. In this work we provide an estimate of the expected bias in the pressure profiles derived from the X-ray and microwave bands taking into account both temperature and density fluctuations in the ICM, as well as the correlation between them. We also predict biases in three-dimensional density and temperature structure derived from X-ray observations. The bias in density depends on the ability (determined by the photon statistics and X-ray background) to mask out X-ray emitting gas clumps in the outskirts of galaxy clusters. Our estimates from section 4.2 seem to suggest that X-ray observations would be able to identify these clumps (if resolved) in clusters up to moderate redshifts ($z \sim 0.1$).

Accurate measurements of the bias as a function of cluster radius will allow us to probe the inhomogeneity and the nature of perturbations (pressure vs. entropy) in the ICM. Our work is also relevant for the use of galaxy clusters in cosmological studies. A robust characterisation of biases between X-ray and SZ observations is critical for constraining cosmological parameters through measurements of the angular diameter distances, d_A, at various redshifts (Bonamente et al. 2006; Khedekar & Majumdar 2010). The
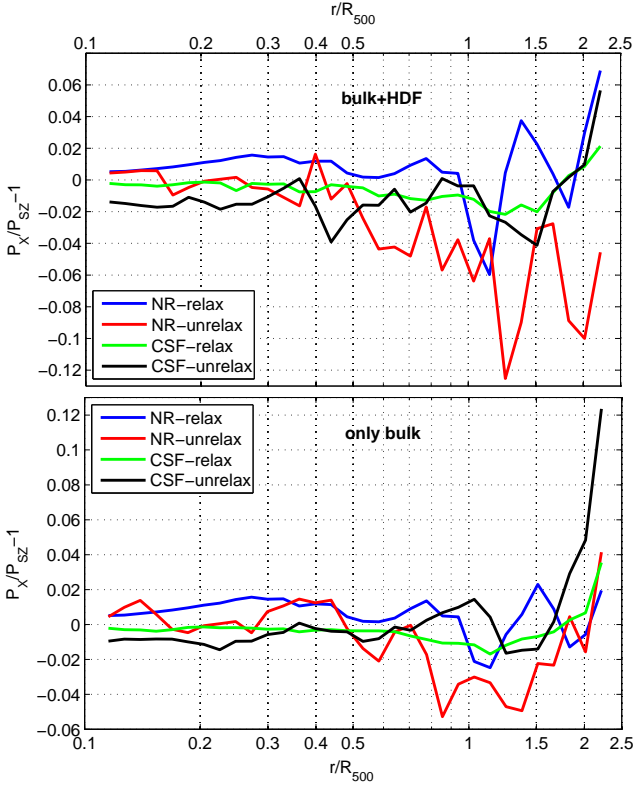
Figure 9. The bias, $b_P(r) \equiv P_X/P_{SZ} - 1$, in pressure profiles for a sample of 16 clusters (both relaxed and unrelaxed) in the NR and CSF simulations. For the figure in lower panel, labelled as 'only bulk', the bias is computed after excluding contributions from the high density fluctuations (HDF) associated with dense clumps.

prediction of the bias in density profiles is also important for the determination of the baryon budget in clusters (e.g., Simionescu et al. 2011; Vazza et al. 2012).

Our results appear to be consistent with the bias (-10% to -40%, from the cluster centre to $r = 0.8\ R_{500}$) in the pressure profiles seen in the Coma cluster (Planck Collaboration, et al. 2012), using data from XMM-Newton and Planck observations. Coma is an unrelaxed cluster and the bias outliers seen in the small sample of unrelaxed simulated clusters range from -15% to $+20\%$ and -60% to $+20\%$, for the NR and CSF simulations respectively, in the same radial range. The current results on the ratio Y_{SZ}/Y_X appear to be mixed and inconsistent with each other. On the one hand, recent observations from the CARMA (Bonamente et al. 2012) indicate that this ratio is consistent with unity, while other measurements (for e.g., Rozo et al. 2012; Andersson et al. 2011) are quite different from the biases derived from our simulations. In our view this is likely due to some underlying systematic uncertainties associated with the interpretation of the current observations (see Bonamente et al. 2006, for a list of possible systematic errors).

Recently, Battaglia et al. (2012b) estimated biases in the gas mass fraction, f_{gas}, derived from X-ray observations, using a set of cosmological cluster simulations. Our results on the bias in the derived gas density from X-ray data due to clumpiness are consistent with their findings. They estimate

the contribution of clumping to $M_{gas}(< R_{200})$ to be $10 - -20\%$ while our results indicate a *median* bias of 16% in the density at the same radius.

6   CONCLUSIONS

The main conclusions of this paper are summarised below:

• We first investigate the dependence of bias between the X-ray and SZ pressures by fitting the X-ray emission from an idealised hot gas having a lognormal distribution of density and temperature values. Our results demonstrate that the bias is expected to be small (within $\pm 10\%$), as long as the magnitude of density and temperature fluctuations is sufficiently small (σ_T, $\sigma_{ne} < 0.45$) and their correlation does not take large negative values ($\xi > -0.3$), for median temperatures, $T_{median} \geqslant 3$ keV. However, the bias may be somewhat larger ($\sim 15\%$) for clusters with lower temperatures ($T_{median} \lesssim 1$ keV). We provide a fitting form to predict the bias as a function of the properties of fluctuations of the ICM for $T_{median} \geqslant 3$ keV and plot bias contours in the (ξ, σ) plane that may be used to probe the properties of fluctuations from a given observed ratio of P_X/P_{SZ}. At lower temperatures ($T_{median} < 3$ keV), the bias is also found to be a function of the metal abundance in the gas.

• We then use a sample of 16 simulated clusters to study properties of the ICM fluctuations. The clusters in the simulations show an increase in the amplitude of both density and temperature fluctuations with radius. The fluctuations of temperature and density are mostly negatively correlated within $r < R_{500}$. This correlation is close to zero at higher radii. We compute P_X and P_{SZ} profiles using the ICM from simulated clusters as would be measured from X-ray and SZ observations. Both P_{SZ} and P_X are biased with respect to the median pressures values. For P_{SZ} this bias is purely due to the asymmetric (near lognormal) distribution of pressure fluctuations; for P_X, in addition to the bias from asymmetry, there is also a bias arising from fitting a single temperature model to the multi-component emission spectrum.

• We show that the median bias, $b_P(r) \equiv P_X(r)/P_{SZ}(r) - 1$, between the pressure estimated from X-ray and SZ observations is small and lies within -6% to +2%, up to R_{500}, even for unrelaxed clusters. The scatter in the pressure bias is significantly smaller for relaxed clusters (< 0.03) than unrelaxed clusters (< 0.13) at $r < R_{500}$; however, it becomes large and positively skewed at $r \sim 2\ R_{500}$. For non-relaxed clusters, there is a noticeably higher scatter in the bias values from shell to shell. The outliers responsible for the scatter in bias can be reduced by almost an order of magnitude just by using a simple method of excluding the brightest clumps (as permitted by reasonably good photon statistics) from the cluster outskirts ($r > R_{500}$), for both relaxed and unrelaxed clusters.

• Finally, our results on the median values of pressure bias between X-ray and SZ observations are not significantly different in the two types of simulations with different input physics: (i) Non-radiative (NR) runs and (ii) Cooling + star formation (CSF) runs. Therefore these results, (i.e. a small bias within R_{500}) may be considered to be robust with respect to possible uncertainties in the physical implementations in the hydro codes.

ACKNOWLEDGEMENTS

REFERENCES

Allen S. W., Evrard A. E., Mantz A. B., 2011, ARA&A, 49, 409
Ameglio S., et al., 2007, MNRAS, 382, 397
Anders E., Grevesse N., 1989, Geochim. Cosmochim. Acta, 53, 197
Andersson K., et al., 2011, ApJ, 738, 48
Battaglia N., et al., 2012a, ApJ, 758, 74
Battaglia N., et al., 2012b, arXiv: 1209.4082
Bonamente M., et al., 2006, ApJ, 647, 25
Bonamente M., et al., 2012, New Journal of Physics, 14, 025010
Buote D. A., Tsai J. C., 1995, ApJ, 452, 522
Burenin R. A., Vikhlinin A. A., 2012, Astronomy Letters, 38, 347
Churazov E., Sazonov S., Sunyaev R., Forman W., Jones C., Böhringer H., 2005, MNRAS, 363, L91
Churazov E., Forman W., Jones C., Böhringer H., 2003, ApJ, 590, 225
Churazov E., et al., 2012, MNRAS, 421, 1123
Croton D. J., et al., 2006, MNRAS, 365, 11
Evrard A. E., et al., 2008, ApJ, 672, 122
Fabian A. C., et al., 1981, ApJ, 248, 47
Fabian A. C., et al., 2006, MNRAS, 366, 417
Gladders M. D., Yee H. K. C., Majumdar S., Barrientos L. F., Hoekstra H., Hall P. B., Infante L., 2007, ApJ, 655, 128
Haiman Z., Mohr J. J., Holder G. P., 2001, ApJ, 553, 545
Inogamov N. A., Sunyaev R. A., 2003, AstL, 29, 791
Kaastra J., 1992, An X-Ray Spectral Code for Optically Thin Plasmas (Internal SRON-Leiden Report, updated version 2.0)
Kawahara H., Suto Y., Kitayama T., Sasaki S., Shimizu M., Rasia E., Dolag K., 2007, ApJ, 659, 257

Khedekar S., Majumdar S., 2010, Phys. Rev. D, 82, 081301
Korngut P. M., et al., 2011, ApJ, 734, 10
Kravtsov A. V., Klypin A., Hoffman Y., 2002, ApJ, 571, 563
Kravtsov A. V., Klypin A. A., Khokhlov A. M., 1997, ApJS, 111, 73
Kravtsov A. V., Vikhlinin A., Nagai D., 2006, ApJ, 650, 128
Kravtsov A. V., Borgani S., 2012, ARA&A, 50, 353
Kriss G. A., Cioffi D. F., Canizares C. R., 1983, ApJ, 272, 439
McLaughlin D. E., 1999, AJ, 117, 2398
Lau E. T., Kravtsov A. V., Nagai D., 2009, ApJ, 705, 1129
Leccardi A., Molendi S., 2008, A&A, 487, 461
Liedahl D. A., Osterheld A. L., Goldstein W. H., 1995, ApJ, 438, L115
Lima M., Hu W., 2005, PhRvD, 72, 043006
Majumdar S., Mohr J. J., 2004, ApJ, 613, 41
Marriage T. A., et al., 2011, ApJ, 737, 61
Mathiesen B., Evrard A. E., Mohr J. J., 1999, ApJ, 520, L21
Mazzotta P., Rasia E., Moscardini L., Tormen G., 2004, MNRAS, 354, 10
Mewe R., Gronenschild E. H. B. M., van den Oord G. H. J., 1985, A&AS, 62, 197
Mewe R., Lemen J. R., van den Oord G. H. J., 1986, A&AS, 65, 511
Motl P. M., et al., 2005, ApJ, 623, L63
Nagai D., 2006, ApJ, 650, 538
Nagai D., Vikhlinin A., Kravtsov A. V., 2007a, ApJ, 655, 98
Nagai D., Kravtsov A. V., Vikhlinin A., 2007b, ApJ, 668, 1
Nagai D., Lau E. T., 2011, ApJ, 731, L10
Noh Y., Cohn J. D., 2012, MNRAS, 426, 1829
Plagge T., et al., 2010, ApJ, 716, 1118
Plagge T. J., et al., 2012, arXiv: 1203.2175
Planck Collaboration, et al., 2011a, A&A, 536, A8
Planck Collaboration, et al. 2011b, arXiv: 1112.5595
Planck Collaboration, et al. 2012, arXiv: 1208.3611
Poole G. B., Fardal M. A., Babul A., McCarthy I. G., Quinn T., Wadsley J., 2006, MNRAS, 373, 881
Rafferty D. A., McNamara B. R., Nulsen P. E. J., Wise M. W., 2006, ApJ, 652, 216
Rapetti D., et al., 2009, MNRAS, 400, 699
Rasia E., et al., 2006, MNRAS, 369, 2013
Reese E. D., et al., 2012, ApJ, 751, 12
Reichardt C. L., et al., 2012, arXiv: 1203.5775
Roncarelli M., Ettori S., Dolag K., Moscardini L., Borgani S., Murante G., 2006, MNRAS, 373, 1339
Rozo E., et al., 2010, ApJ, 708, 645
Rozo E., Vikhlinin A., More S., 2012, arXiv: 1202.2150
Russell H. R., Sanders J. S., Fabian A. C., 2008, MNRAS, 390, 1207
Sayers J., et al., 2012, arXiv, arXiv:1211.1632
Simionescu A., et al., 2011, Science, 331, 1576
Smith R. K., Brickhouse N. S., Liedahl D. A., Raymond J. C., 2001, ApJ, 556, L91
Somerville R. S., Hopkins P. F., Cox T. J., Robertson B. E., Hernquist L., 2008, MNRAS, 391, 481
Sunyaev R. A., Zeldovich Y. B., 1972a, A&A, 20, 189

Sunyaev R. A., Zeldovich Y. B., 1972b, Comments on Astrophysics and Space Physics, 4, 173

Vazza F., Roncarelli M., Ettori S., Dolag K., 2011, MNRAS, 413, 2305

Vazza F., Eckert D., Simionescu A., Brüggen M., Ettori S., 2012, MNRAS, 308

Vikhlinin A., Kravtsov A., Forman W., Jones C., Markevitch M., Murray S. S., Van Speybroeck L., 2006, ApJ, 640, 691

Vikhlinin A., et al., 2009, ApJ, 692, 1060

Zhang Y.-Y., et al., 2009, ApJ, 699, 1178

Zhuravleva I., Churazov E., Kravtsov A., Sunyaev R., 2012a, MNRAS, 422, 2712

Zhuravleva I., Churazov E., Kravtsov A., Lau E. T., Nagai D., Sunyaev R., 2012b, MNRAS, 428, 3274

This paper has been typeset from a TEX/ LATEX file prepared by the author.